Supplementary Information

# Two-dimensional (2D) layered double metal cyanide as catalysts for $CO_2$-epoxide copolymerization

*Guillermo Penche[a], María P. González-Marcos*[a], Juan R. González-Velasco[a], Cyler W. Vos[b], Christopher M. Kozak[b]*

[a]Department of Chemical Engineering, Faculty of Science and Technology, University of the Basque Country, UPV/EHU, Barrio Sarriena s/n, 48940-Leioa, Bizkaia, Spain

[b]Department of Chemistry, Memorial University of Newfoundland, St. John's, NL, Canada A1B 3X7.

*Corresponding author. e-mail: mp.gonzalezmarcos@ehu.eus

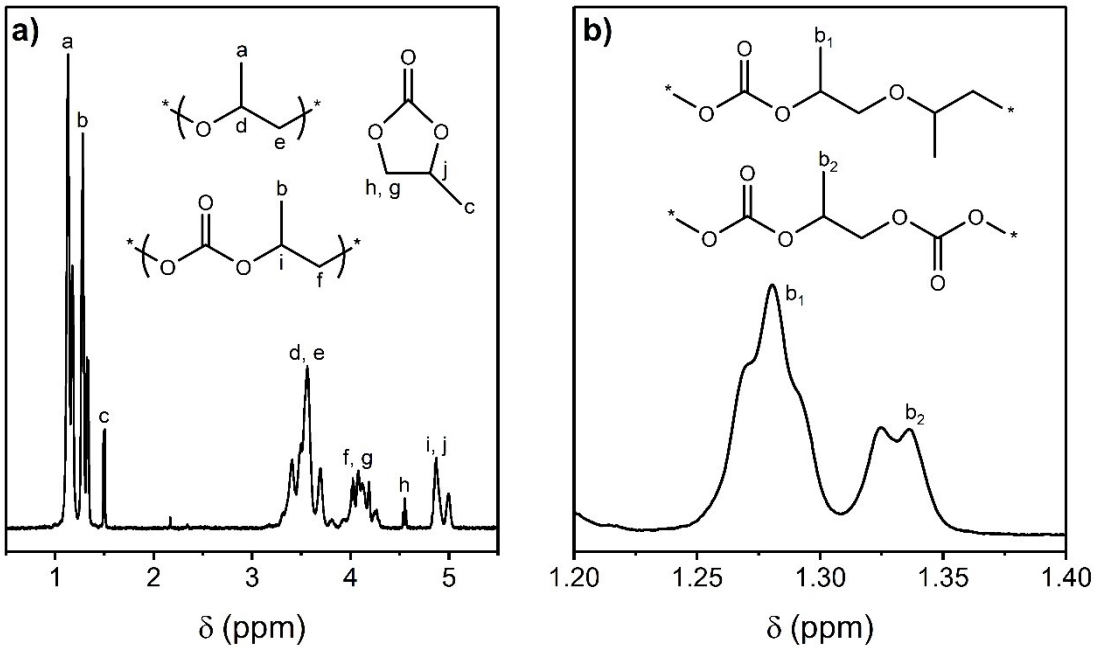


**Fig. S1.** Assignment of the $^1$H-NMR spectrum of a typical product of the copolymerization of $CO_2$ and PO in the presence of a DMC catalyst; **a)** Full spectrum and **b)** region between 1.2 ppm and 1.4 ppm.

$F_{CU}$ was calculated by integration of the methyl resonances of polyether (1.14 ppm) and polycarbonate segments (1.3 ppm).

$$F_{CU}, \text{mol\%} = \frac{A_{1.3}}{A_{1.3} + A_{1.14}} \cdot 100 \qquad \text{(S1)}$$

$W_{PC}$ was determined considering the methyl resonance of PC (1.48 ppm).

$$W_{PC}, \text{wt.\%} = \frac{102 \cdot A_{1.48}}{58 \cdot A_{1.14} + 102 \cdot (A_{1.3} - A_{1.48})} \cdot 100 \qquad \text{(S2)}$$

$S_{CO2}$ and $S_{PO}$ were calculated by integrating all the NMR signals in the $CH_3$ region.

$$S_{CO2}, \% = \frac{A_{1.3}}{A_{1.3} + A_{1.48}} \cdot 100 \qquad \text{(S4)}$$

$$S_{PO}, \% = \frac{A_{1.14} + A_{1.3}}{A_{1.14} + A_{1.3} + A_{1.48}} \cdot 100 \qquad \text{(S5)}$$

$R_{PEC}$ was estimated from the two different resonances into which the signal corresponding to the $CH_3$ protons in polycarbonate units (1.3 ppm) can be decomposed, following the formula:

$$R_{PEC}, \% = \frac{A_{1.28}}{A_{1.28} + A_{1.33}} \cdot 100 \quad \text{(S6)}$$

In a block copolymer, polyethercarbonate linkages would be limited to the block interface, resulting in a $R_{PEC}$ value approaching 0%. Conversely, for a copolymer with a more random microstructure, this value should be closer to 100%.

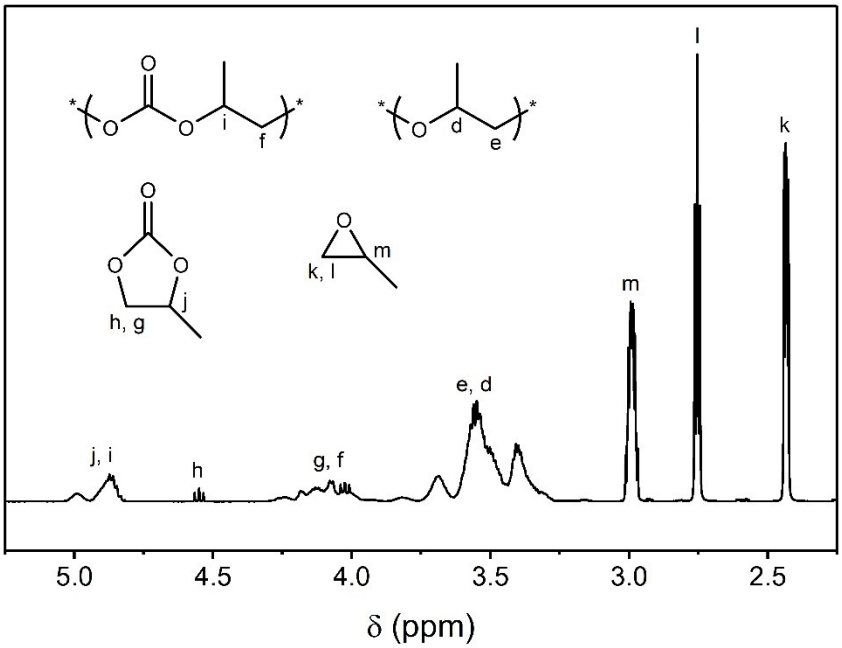


**Fig. S2.** Representative $^1$H-NMR spectrum of the fresh product of the copolymerization of $CO_2$ and PO in the presence of a DMC catalyst.

$X_{PO}$ conversion is determined by dividing copolymer and PC peaks integration by the sum of copolymer, PC and PO peaks integrations.

$$X_{PO}, \% = \frac{A_{5.0} + A_{4.58} + A_{4.2} + A_{3.5}}{A_{5.0} + A_{4.58} + A_{4.2} + A_{3.5} + 3 \cdot A_{3.0}} \cdot 100 \quad \text{(S7)}$$

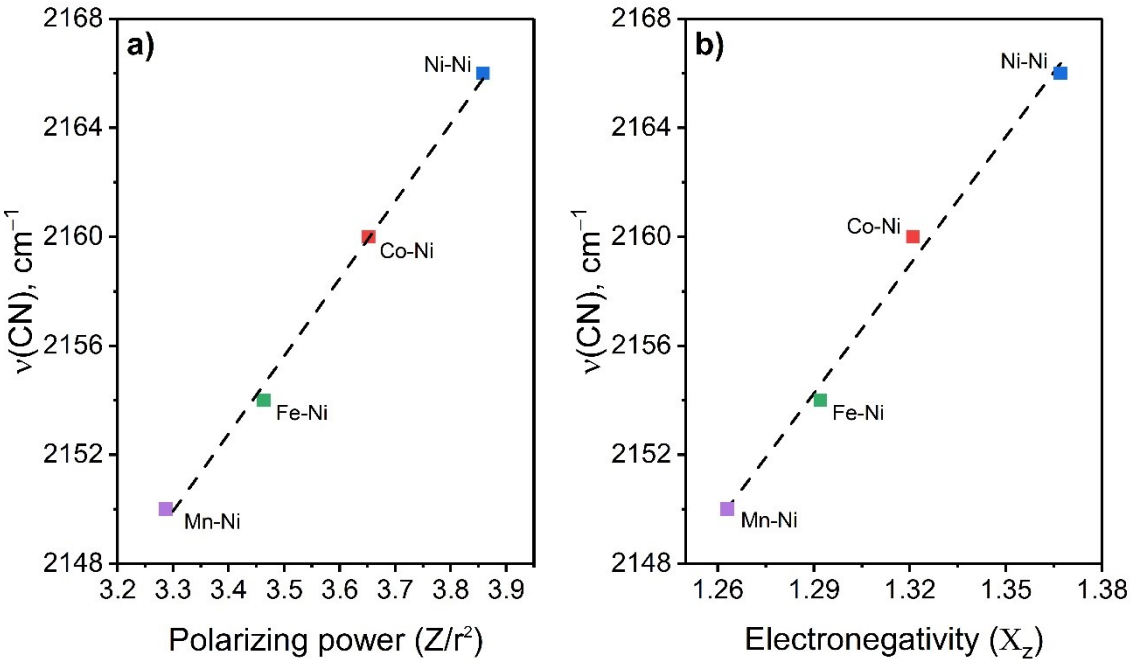


**Fig. S3.** Relationship between the ν(CN) band frequency in the 2D layered DMCs and **a)** the polarizing power of the M′ metal ($R^2$=0.9962) or **b)** the electronegativity of the M′ metal ($R^2$= 0.9918). Electronegativity and polarizing power values extracted from Zhang's work.[1,2]

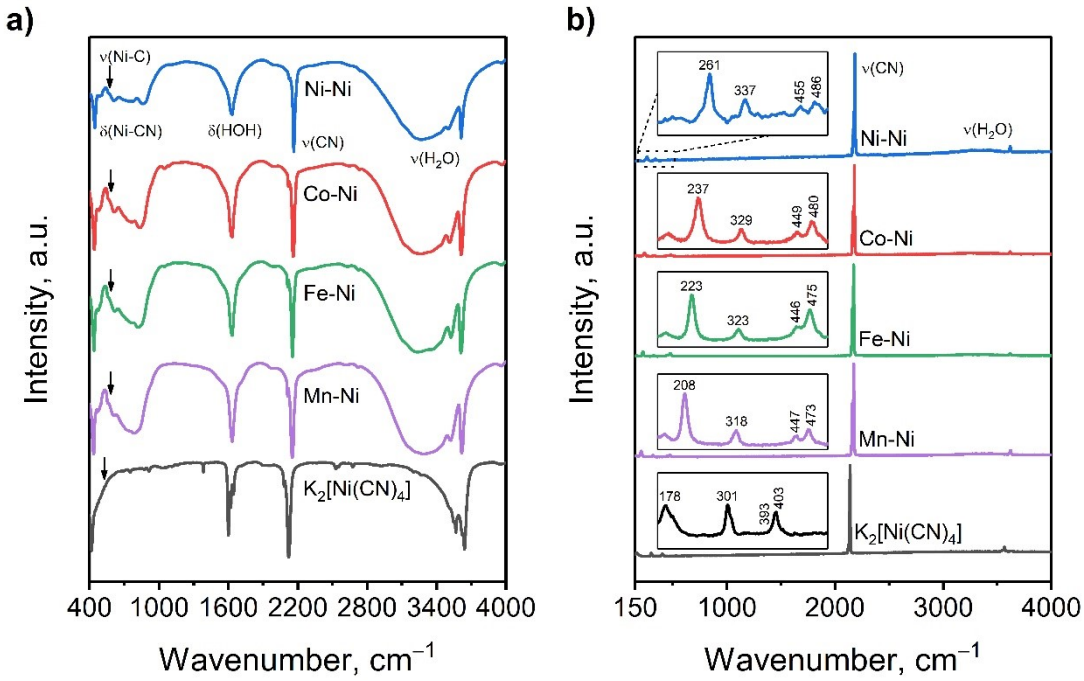


**Fig. S4.** Full vibrational **a)** Infrared and **b)** Raman spectra of the studied 2D layered DMC materials in the hexahydrate form. Insets: Raman low-frequency spectral region.

FT-IR and Raman spectra of the synthesized compounds comprise motions associated with the $[Ni(CN)_4]^{2-}$ ion and water molecules. The free $[Ni(CN)_4]^{2-}$ is a square planar ion with $D_{4h}$ symmetry, consisting of 9 atoms and 21 fundamental modes. Those vibrational modes can be Raman active, IR active, or neither. The wavenumbers of IR and Raman vibrations related to the $[Ni(CN)_4]^{2-}$ are listed in **Table S1**. Assignments were made based on the bibliography.[3] As in the case of the ν(CN), bands in the low-frequency regions shift to higher wavenumbers with the electron-withdrawing capacity of the M′ metal.

**Table S1.** Assignment of the vibration modes related to the square planar $[Ni(CN)_4]^{2-}$ ion.

| | $K_2[Ni(CN)_4]$ | $Ni[Ni(CN)_4]$ | $Co[Ni(CN)_4]$ | $Fe[Ni(CN)_4]$ | $Mn[Ni(CN)_4]$ |
|---|---|---|---|---|---|
| ν(CN), $A_{1g}$ (R) | 2140 s | 2184 s | 2179 s | 2173 s | 2171 s |
| ν(CN), $B_{1g}$ (R) | 2134 m | 2173 m | 2167 m | 2161 m | 2159 m |
| ν(CN), $E_u$ (IR) | 2122 s | 2166 s | 2160 s | 2154 s | 2152 s |
| ν(Ni-C), $A_{1g}$ (R) | 403 w | 486 w | 480 w | 475 w | 473 w |
| ν(Ni-C), $B_{1g}$ (R) | 393 w | 455 w | 449 w | 446 w | 447 w |
| δ(Ni-CN), $B_{2g}$ (R) | 178 w | 261 w | 237 w | 223 w | 208 w |
| π(Ni-CN), $E_g$ (R) | 301 w | 337 w | 329 w | 323 w | 318 w |
| ν(Ni-C), $E_u$ (IR) | 543 w | 567 w | 561 w | 560 w | 558 w |
| δ(Ni-CN), $E_u$ (IR) | 418 s | 450 s | 442 s | 439 s | 435 s |
| π(Ni-CN), $A_{2u}$ (IR) | 441 w | 482 w | 482 w | 477 w | 473 w |

m: medium; w: weak; s: strong

The presence of crystal water is indicated by ν(OH) and δ(HOH) motions, as well as weak to medium intensity bands between 450-900 $cm^{-1}$, assigned to the rocking and wagging modes of $H_2O$. In the ν(OH) region, three adsorption bands emerge: a broad, weak band due to hydrogen-bonded water molecules, and two sharp, strong bands due to coordinated water. The highest frequency band corresponds to water molecules directly coordinated with the M′ metal, while the intermediate frequency band is associated with water molecules loosely bound to the Ni atoms of the $[Ni(CN)_4]^{2-}$ blocks. It is important to note that these spectra represent hexahydrate form of the synthesized materials, consistent with the observed three types of water molecules. No TBA was detected in the IR spectra.

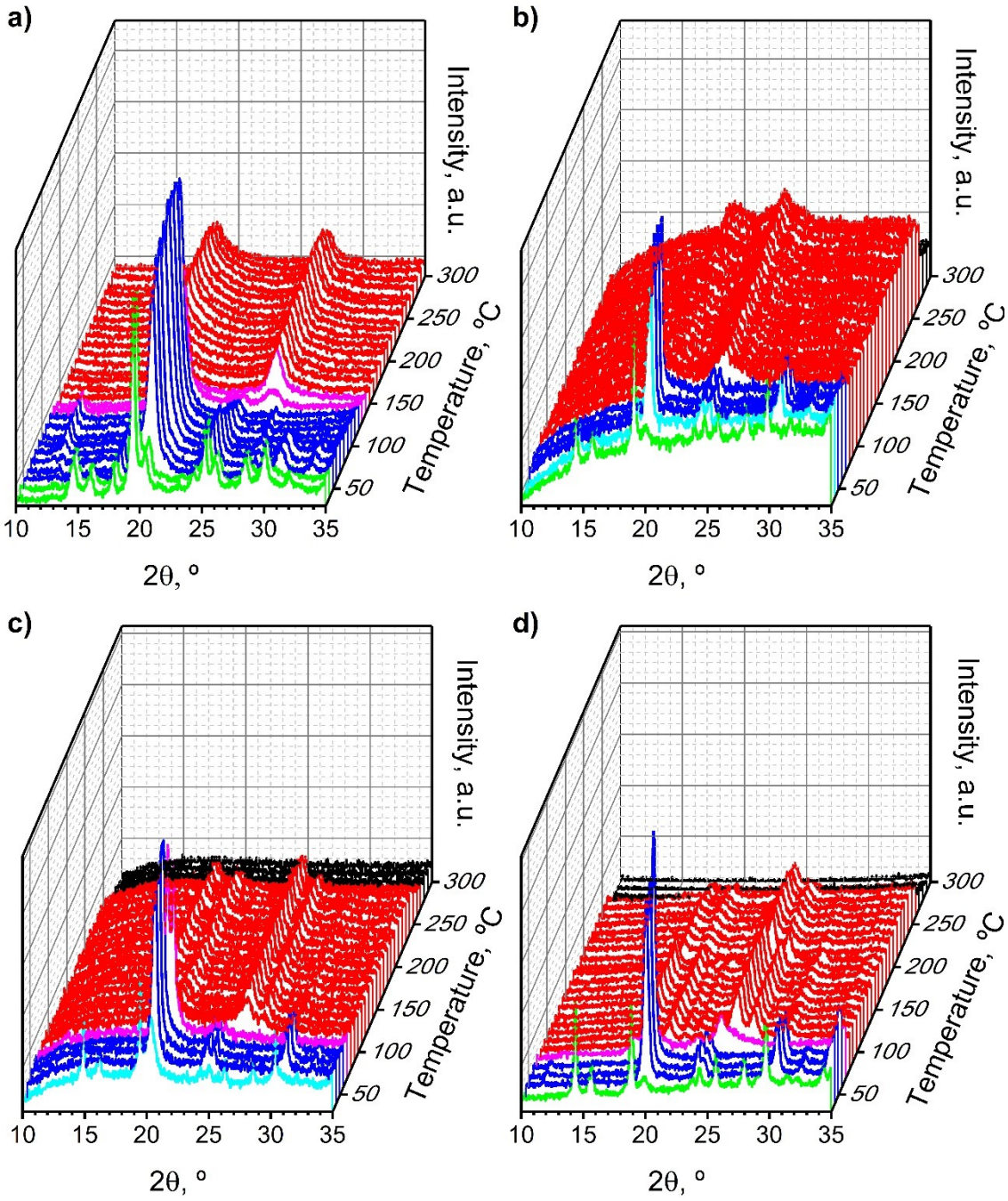


**Fig. S5.** HT-XRD plots of the synthesized 2D layered DMC materials in air: **a)** Ni-Ni, **b)** Co-Ni, **c)** Fe-Ni and **d)** Mn-Ni. Color code: green (hexahydrate form), cyan (mix of hexa- and trihydrate forms), blue (trihydrate form), magenta (mix of tri- and dehydrated forms), red (dehydrated form), and black (product of decomposition).

Above 300 ºC, all crystalline phases degrade, except for the Ni-Ni sample, which remains stable up to 310 ºC. The rest of the samples degrade at 280 ºC (Co-Ni) and 260 ºC (Fe-Ni and Mn-Ni). Notably, a linear correlation exists between the degradation temperature and the C≡N stretching vibrational energy ($R^2$= 0.9843) which essentially measures the bond strength of the Ni-C≡N-M′ chain.

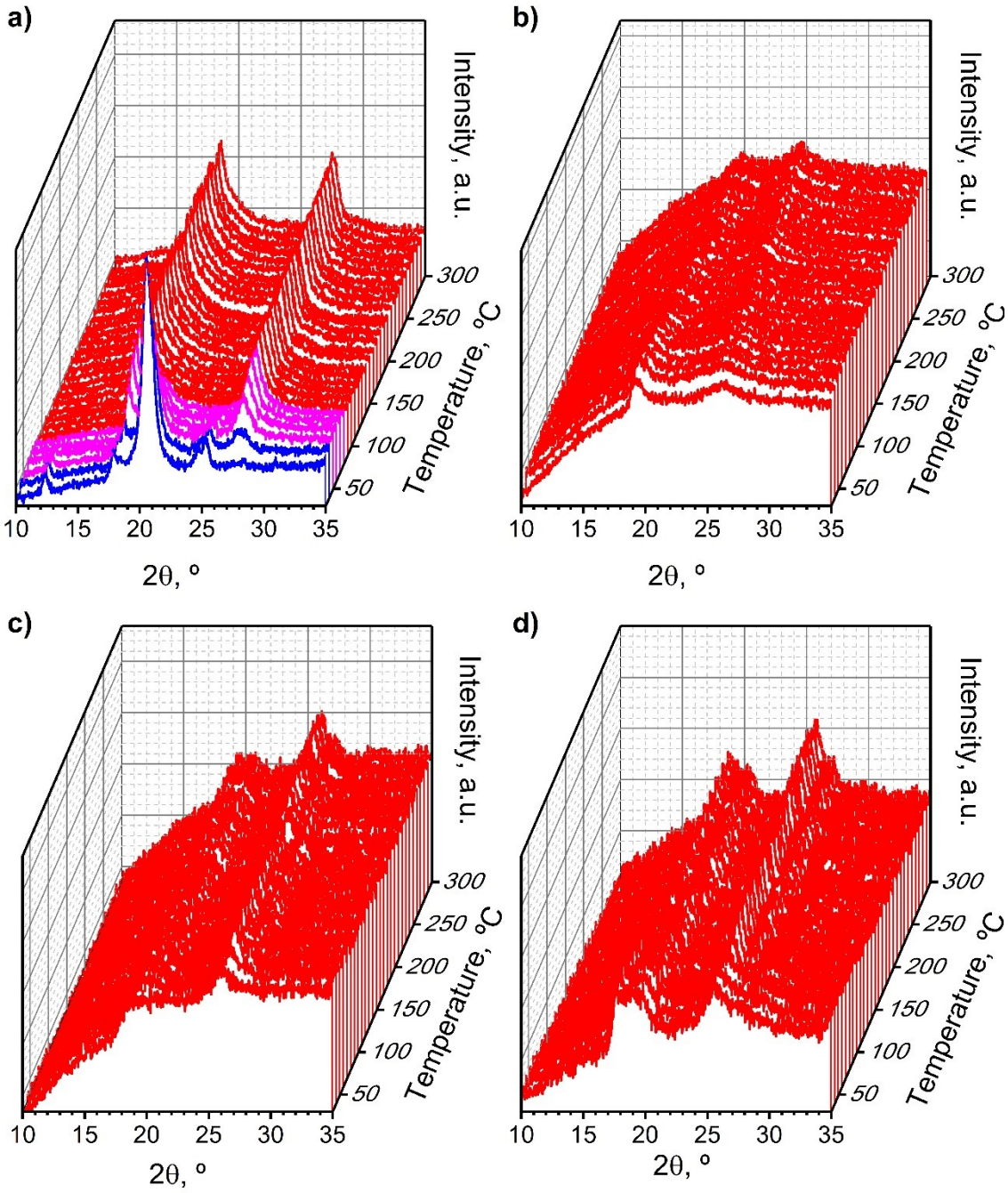


**Fig. S6.** HT-XRD plots of the synthesized 2D layered DMC materials in vacuum: **a)** Ni-Ni, **b)** Co-Ni, **c)** Fe-Ni, and **d)** Mn-Ni. Color code: blue (trihydrate form), magenta (mix of tri- and dehydrated forms) and red (dehydrated form).

Although dehydration occurs at low temperatures in vacuum, decomposition takes place at significantly higher temperatures than in air, with all samples remaining stable even at 400 ºC. This difference in the decomposition temperature arises from distinct decomposition mechanism in air and vacuum. In air, DMCs oxidize to metal oxides, whereas in inert atmospheres, they reduce to pure metals and metal carbides.[4,5]

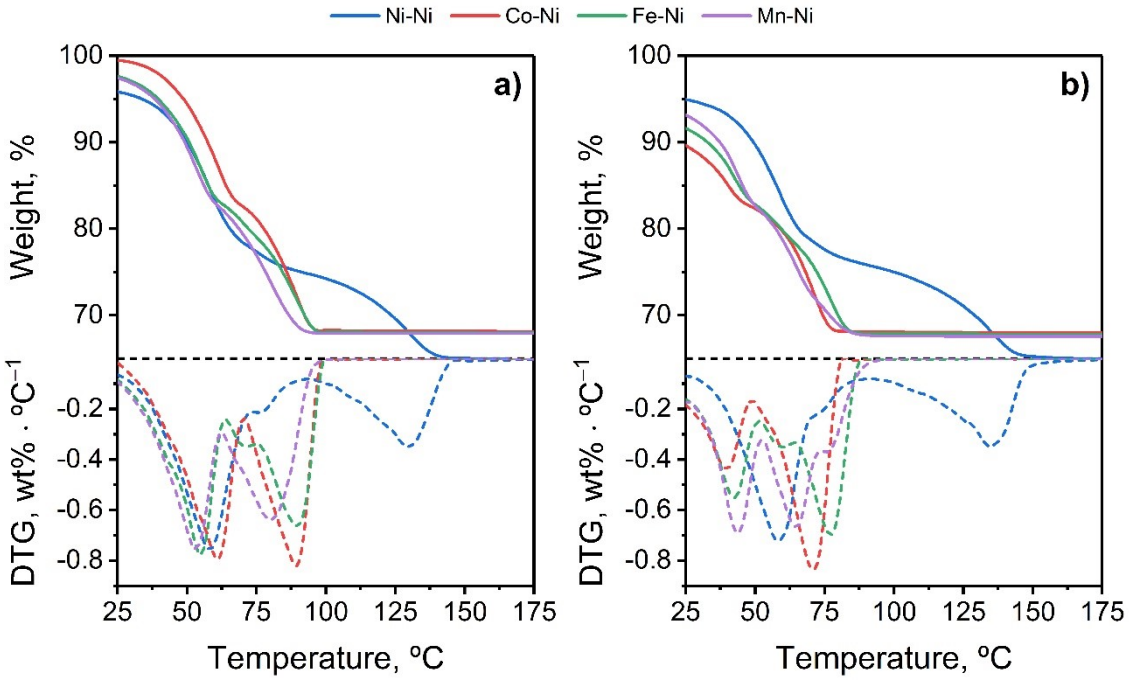


**Fig. S7**. TGA curves of the studied 2D layered DMC materials in the range between 25 ºC and 175 ºC in **a)** air and **b)** $N_2$.

**Fig. S7** provides a detailed view of the stages of water weight loss. In the second stage, two additional weight losses can be slightly differentiated, one corresponding to coordinated water and the other to weakly linked water. However, the inflection point is not well-defined. In $N_2$, water is released even at room temperature.

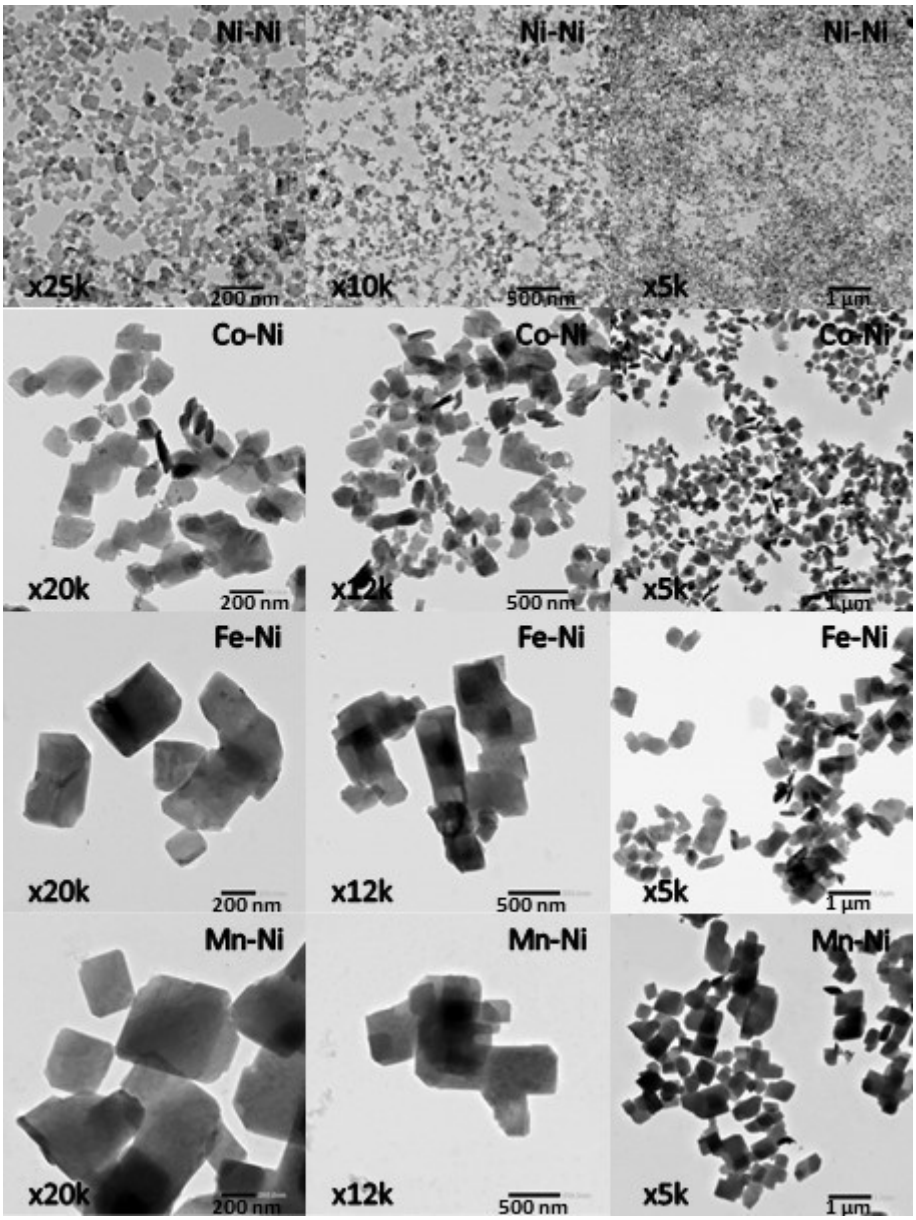


**Fig. S8.** TEM images of the studied 2D layered DMC materials at different magnifications.

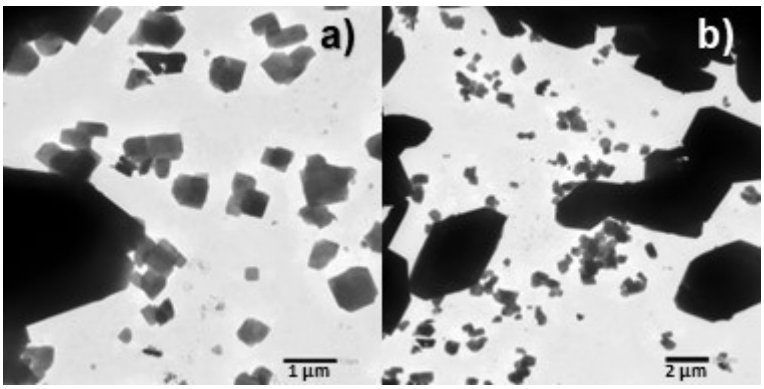


**Fig. S9.** TEM images of the Mn-Ni sample at **a)** 5000 and **b)** 2000 magnifications.

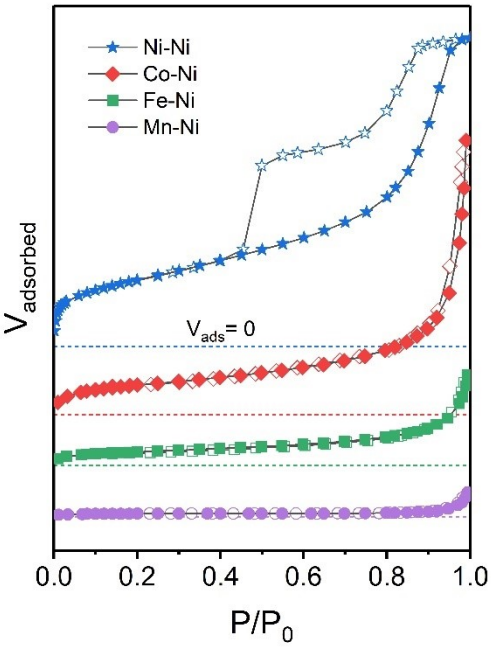


**Fig. S10.** $N_2$ adsorption-desorption isotherms of the studied 2D layered DMC materials.

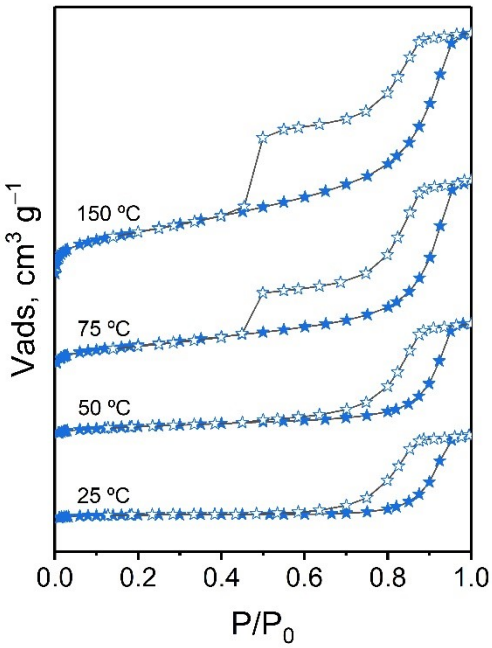


**Fig. S11.** $N_2$ adsorption-desorption isotherms of the Ni-Ni sample at different pretreatment temperatures.

**Table S2.** Textural properties of the Ni-Ni sample at different pretreatment temperatures.

| $T_{pre}$, ºC | $S_{BET}$, $m^2$ $g^{-1}$ | $V_p$, $cm^3$ $g^{-1}$ | $D_p$[a], nm | $D_p$[b], nm |
|---|---|---|---|---|
| 25 | 11.6 | 0.0463 | 20.5 | 11.7 |
| 50 | 17.0 | 0.0601 | 18.6 | 10.4 |
| 75 | 40.6 | 0.1035 | 12.7 | 6.9 |
| 150 | 70.4 | 0.1345 | 8.7 | 5.3 |

[a] Determined from the BJH method applied to the adsorption branch.
[b] Determined from the BJH method applied to the desorption branch.

At low dehydration temperatures, the Ni-Ni sample displays a H2(b) hysteresis loop characteristic of complex porous structures with pore blocking affected desorption. As pretreatment temperature increases, a reduction in pore neck diameter is observed, leading to a pronounced step down in the hysteresis loop due to cavitation. The desorption branch-determined pore size is influenced by pore network effects, and it corresponds to the pore entrances, while the adsorption branch offers a more reliable pore size distribution. The increase in the specific surface area ($S_{BET}$) and pore volume ($V_p$) values, along with the decrease in pore diameter ($D_p$) with pretreatment temperature, suggests that dehydration after thermal treatment results in more compact and porous Ni-Ni particle agglomerates.

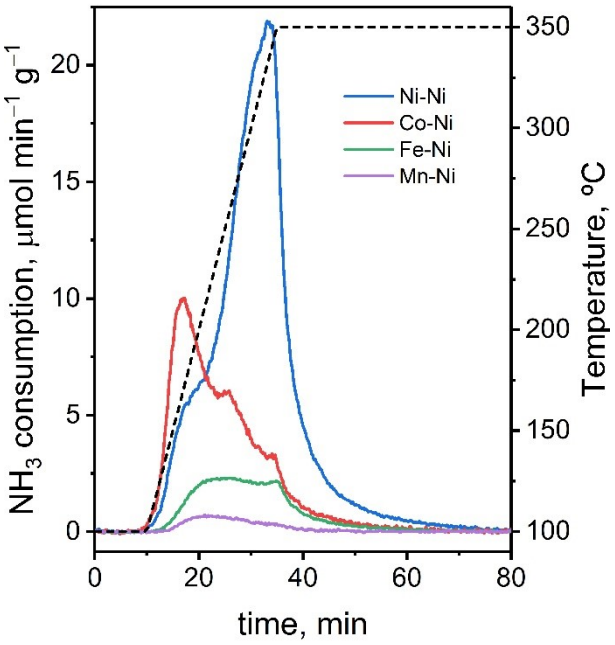


**Fig. S12.** $NH_3$-TPD profiles of the studied 2D layered DMC materials in the temperature range between 100 and 350 ºC.

Some samples exhibit a peak truncated at 350 ºC, which indicates that some $NH_3$ might be lost at higher temperatures. **Table S3** presents the acid site strength distribution, using a 225 ºC threshold temperature as an arbitrary criterion to differentiate weak and strong acid centers. In terms of percentage, the acid center strength decreases in the following order: Ni-Ni>Mn-Ni≈Fe-Ni>Co-Ni.

**Table S3.** Acid sites strength distribution for the studied 2D layered DMC materials.

| Catalyst | Acid Sites strength, µmol $NH_3$ $g^{-1}$ | |
|---|---|---|
| | Weak[a] | Strong[b] |
| Ni-Ni | 53 | 277 |
| Co-Ni | 81 | 73 |
| Fe-Ni | 24 | 30 |
| Mn-Ni | 5 | 7 |

[a] Acid sites between 100 ºC and 225 ºC.
[b] Acid sites between 225 ºC and 350 ºC.

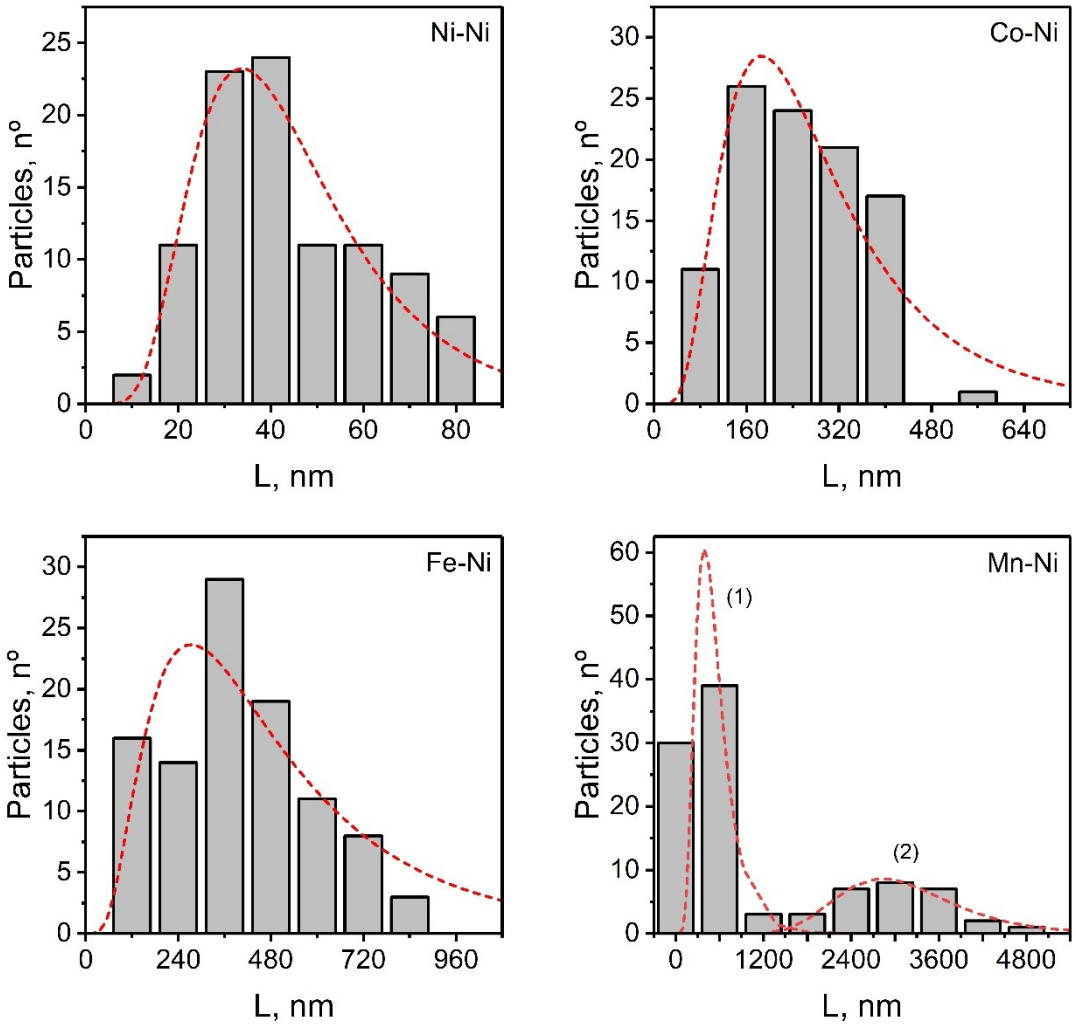


**Fig. S13**. Number-weighted in-plane size (L) distribution of the studied 2D layered DMC materials.

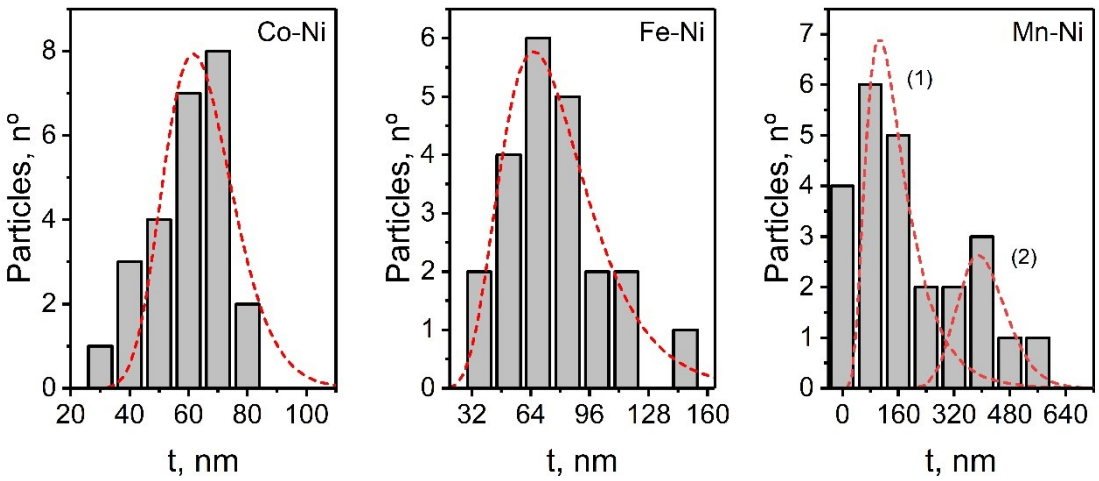


**Fig. S14.** Number-weighted lateral size (t) distribution of the studied 2D layered DMC materials.

Number-weighted particle size distribution (PSD) was conducted using TEM images and ImageJ software. The ferret diameter of particles defined the length (L), while the minimum distance between the lateral face edges defined the thickness (t). For L measurements, 100 particles were counted, while for t measurements, 20 to 25 particles were counted. Data was fitted to the log-normal distribution. **Table S4** shows the most relevant statistical parameters.

**Table S4.** Mode, median, mean (μ), standard deviation (σ), standard error (SE) and R-squared ($R^2$) of the fitted peaks.

| Sample | Measurement | Mode | Median | μ | σ | SE | $R^2$ |
|---|---|---|---|---|---|---|---|
| Ni-Ni | L | 34 | 41 | 46 | 21.98 | 2.19 | 0.9076 |
| | t | - | - | - | - | - | - |
| Co-Ni | L | 189 | 253 | 295 | 177.14 | 17.71 | 0.8826 |
| | t | 62 | 64 | 65 | 12.29 | 2.45 | 0.8407 |
| Fe-Ni | L | 273 | 422 | 525 | 388.46 | 38.85 | 0.7281 |
| | t | 65 | 74 | 79 | 28.32 | 6.04 | 0.9268 |
| Mn-Ni | L | 397 | 482 | 535 | 258.99 | 30.52 | 0.9972 |
| | | 2818 | 3030 | 3144 | 870.03 | 164.00 | |
| | t | 106 | 137 | 157 | 85.92 | 28.64 | 0.9827 |
| | | 391 | 402 | 408 | 72.46 | 32.41 | |

**Table S5.** Comparison between experimental and expected values for surface area and acid sites density.

| Surface area, $m^2\ g^{-1}$ | | | Acid sites density, $\mu mol\ m^{-2}$ | | |
|---|---|---|---|---|---|
| Experimental | Geometric | $e_{abs}$[a] | Experimental | Calculated | $e_{abs}$[a] |
| 70.4 | 118.0 | 47.6 | 4.68 | 3.24 | 1.44 |
| 39.7 | 37.0 | 2.7 | 3.87 | 3.19 | 0.68 |
| 14.5 | 28.1 | 13.6 | 3.72 | 3.12 | 0.59 |
| 3.4 | 5.4 | 2.0 | 3.51 | 3.07 | 0.44 |

[a] Absolute error measured as the absolute difference between experimental and calculated values.

To calculate the geometric external surface area, the values of $S_P$ and $V_P$ extracted from TEM images (see **Table 2**) were used. As the samples are expected to be in their dehydrated form during TEM, $N_2$ physisorption, and $NH_3$-TPD analyses, the solid density ($\rho_{cal}$) was determined based on the crystal structure of the trihydrate form, excluding water molecules. The crystal structure of the dehydrated form was not employed for calculations, as it exhibits short-range order and is even unresolved for some samples considered here. For the Mn-Ni sample, the dimensions of the largest particles were used to determine the geometric external surface area. The density of surface M′ metal sites, or the density of surface acid sites, was calculated from the crystal structure of the trihydrate phase. The unit cell dimensions were obtained from the XRD peak positions in patterns corresponding to the trihydrate form. To establish the position of the (002) plane, profile modeling was conducted in the corresponding angular region. **Table S6** shows some resolved crystallographic details.

The reason why the calculated acid site density values are lower than the experimental ones is that the calculations only consider the surface of the sheets, excluding defects, grain boundaries, and even the lateral sides of the particles. The absolute error is particularly high in the Ni-Ni sample, where surface defect density is expected to be higher and the $r_P$ value is close to one. For specific surface areas, the absolute error between measured and calculated values can be attributed to particle agglomeration and the divergence between the actual sample density and that determined from the trihydrate model without water molecules. Although the latter may be a reasonable approximation, upon dehydration, 2D layered DMC complexes undergo negative thermal expansion within the sheets and a reduction in interlayer space, resulting in an increased particle density and consequently lower specific surface area values.

**Table S6.** Unit cell parameters, cell volume and calculated density of the trihydrate form used for calculations.

| Catalysts | Cell parameters, Å | | V, Å$^3$ | $\rho_{cal}$[a], g cm$^{-3}$ |
|---|---|---|---|---|
| Ni-Ni | a: | 7.087 | 871 | 1.404 |
| | b: | 14.102 | | |
| | c: | 8.714 | | |
| Co-Ni | a: | 7.160 | 910 | 1.346 |
| | b: | 14.423 | | |
| | c: | 8.811 | | |
| Fe-Ni | a: | 7.273 | 936 | 1.281 |
| | b: | 14.432 | | |
| | c: | 8.918 | | |
| Mn-Ni | a: | 7.330 | 960 | 1.241 |
| | b: | 14.534 | | |
| | c: | 9.013 | | |

[a] Calculated unit cell density omitting water molecules.

**Table S7.** Chemical composition (in wt%) of the studied 2D layered DMC materials.

| Sample | M′[a] | M[a] | Cl[a] | M′/M, at. at.$^{-1}$ | C[b] | N[b] | C/N, at. at.$^{-1}$ | Estimated catalyst formulation |
|---|---|---|---|---|---|---|---|---|
| Ni-Ni | M′=M: 56.4 | | 3.8 | - | 19.2 | 20.7 | 1.08 | - |
| Co-Ni | 26.0 | 26.5 | 0.9 | 0.98 | 22.0 | 24.5 | 1.05 | $Co_{0.98}[Ni(CN)_{4.07}]Cl_{0.06}$ |
| Fe-Ni | 20.2 | 28.9 | 0.2 | 0.74 | 24.5 | 26.2 | 1.09 | $Fe_{0.74}[Ni(CN)_{3.80}]Cl_{0.01}$ |
| Mn-Ni | 19.5 | 28.5 | 0.2 | 0.73 | 25.1 | 26.7 | 1.10 | $Mn_{0.73}[Ni(CN)_{3.93}]Cl_{0.01}$ |

[a] Determined from WDFRX and adjusted based on C and N values.
[b] Determined from elemental analysis.

WDXRF is a semi-quantitative technique. Therefore, inorganic content was adjusted based on C and N values derived from elemental analysis.

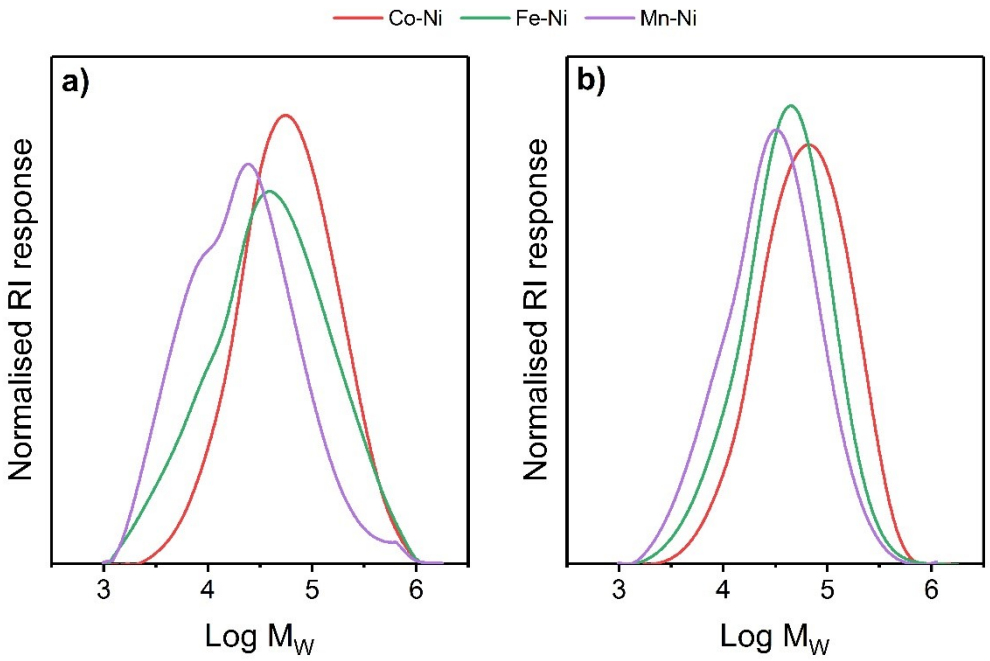


**Fig. S15.** SEC curves (log $M_W$) of the copolymers produced by the studied 2D layered materials. **a)** At 90 ºC and **b)** at 120 ºC.

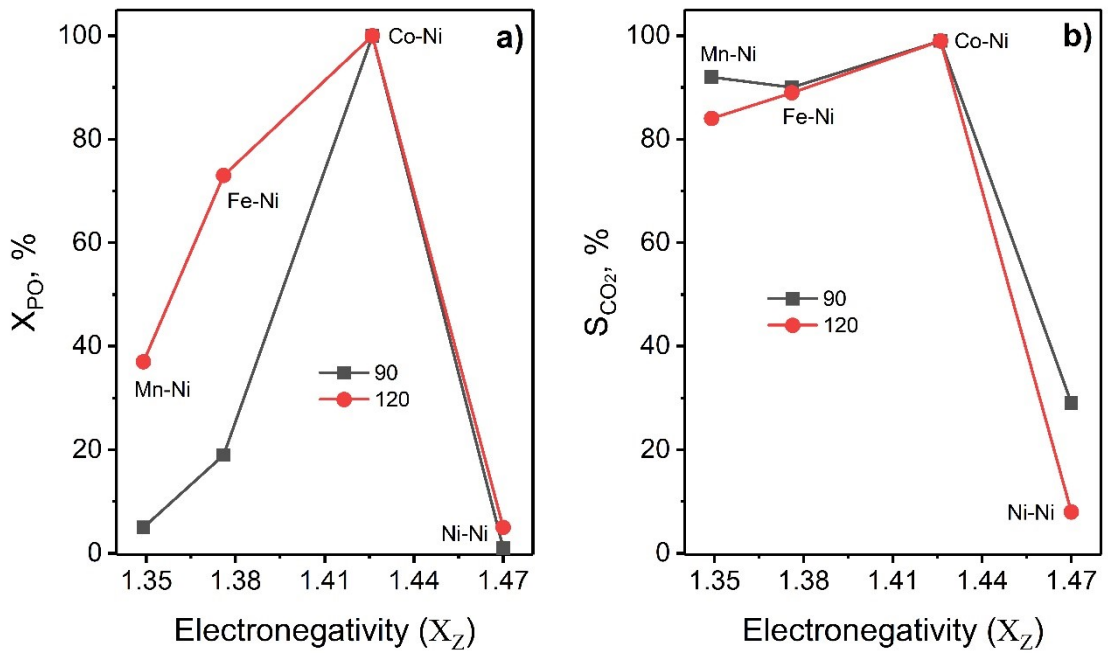


**Fig. S16**. Relationship between electronegativity of the M′ metal and a) PO conversion and b) $CO_2$ selectivity. Electronegativity values were extracted from the Zhang scale.[1]

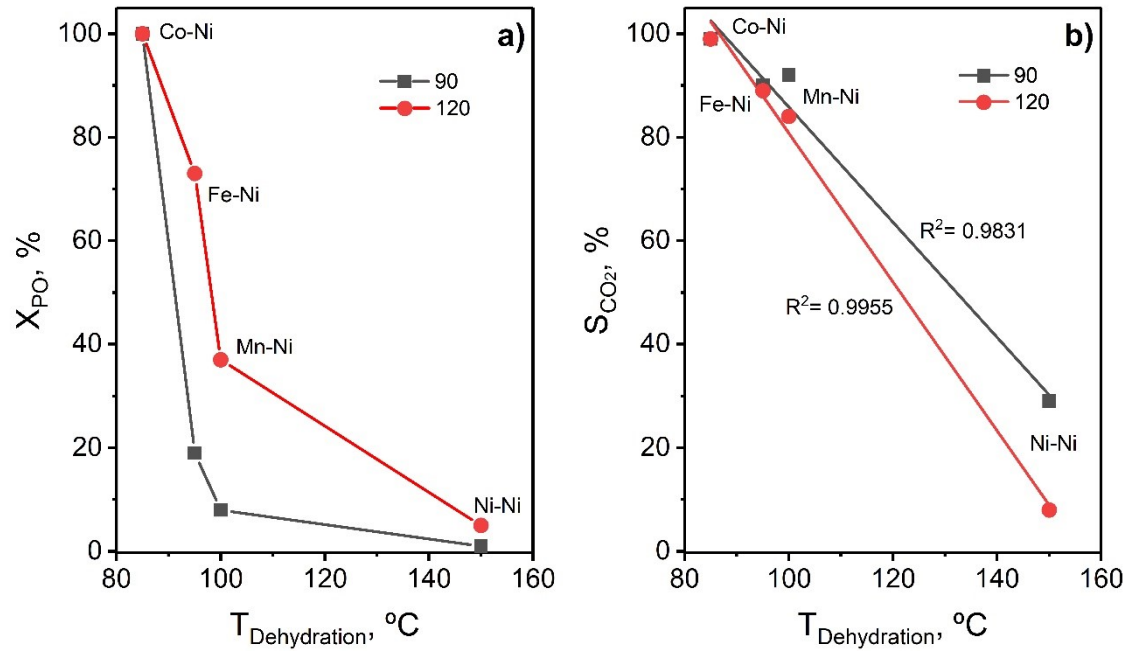


**Fig. S17.** Relationship between dehydration temperature and **a)** PO conversion and **b)** $CO_2$ selectivity.

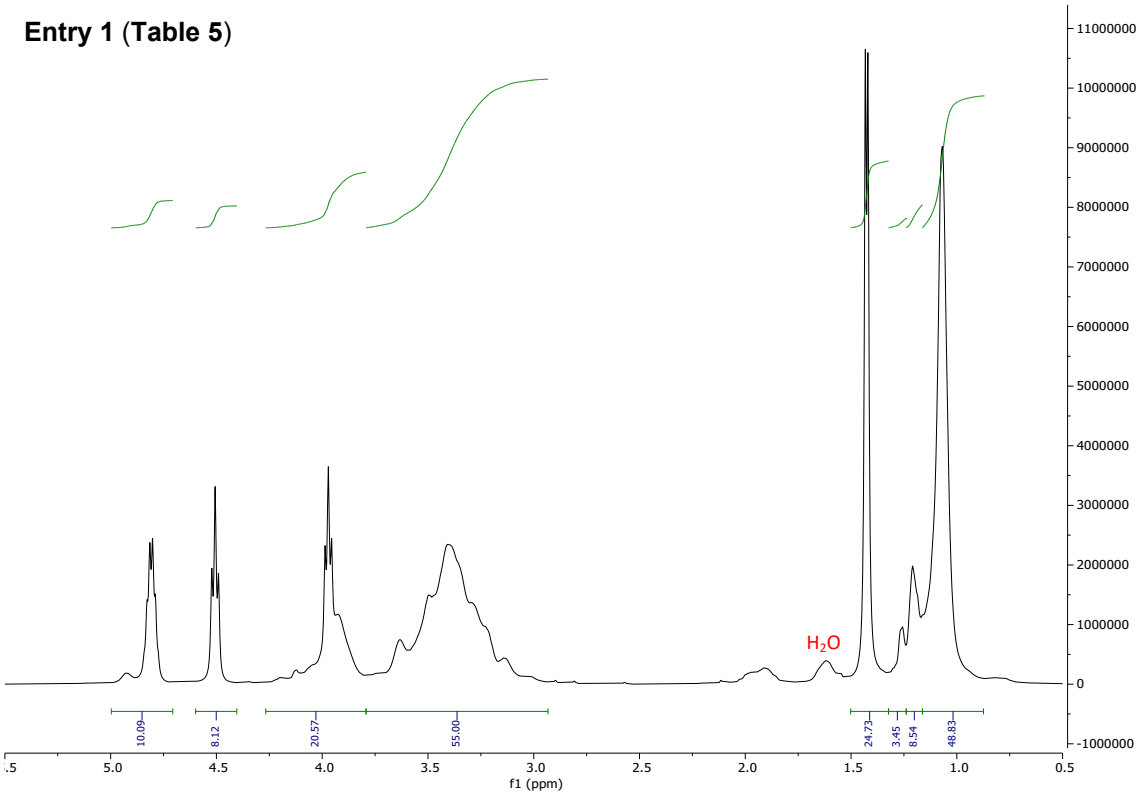


**Fig. S18.** $^{1}$H-NMR spectrum of the product derived from the Ni-Ni catalyst at 90 ºC.

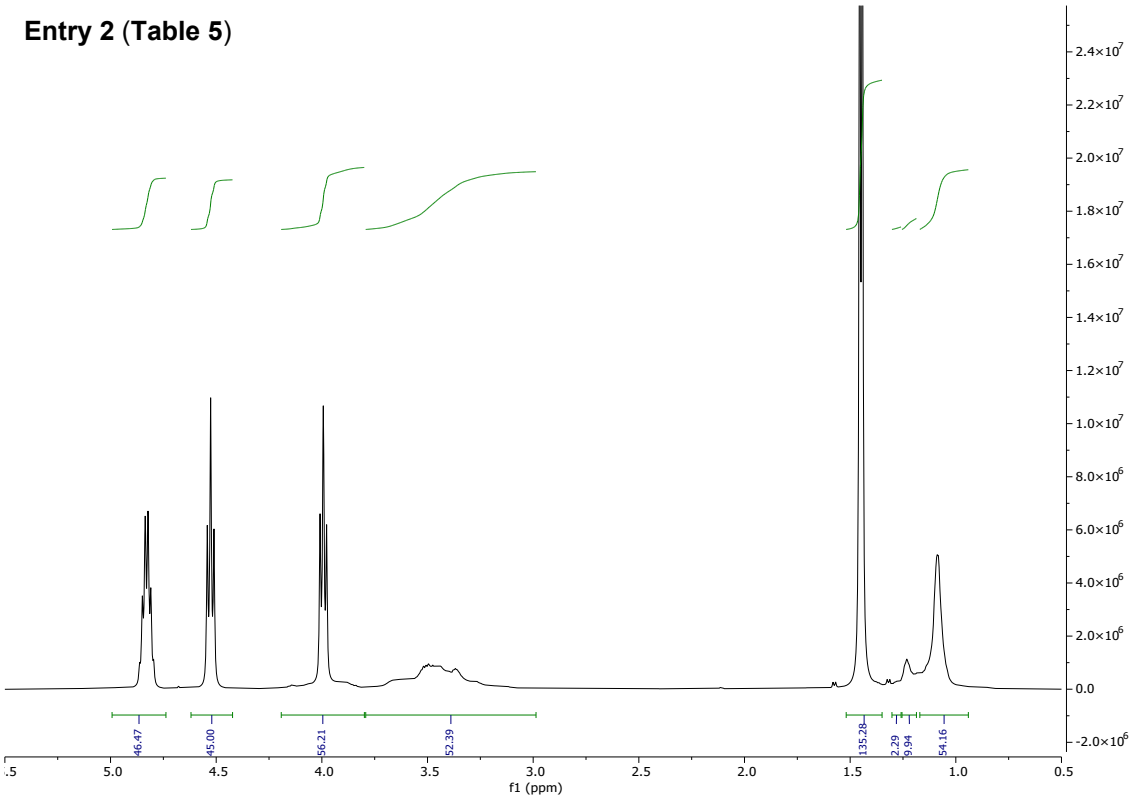


**Fig. S19.** $^{1}$H-NMR spectrum of the product derived from the Ni-Ni catalyst at 120 ºC.

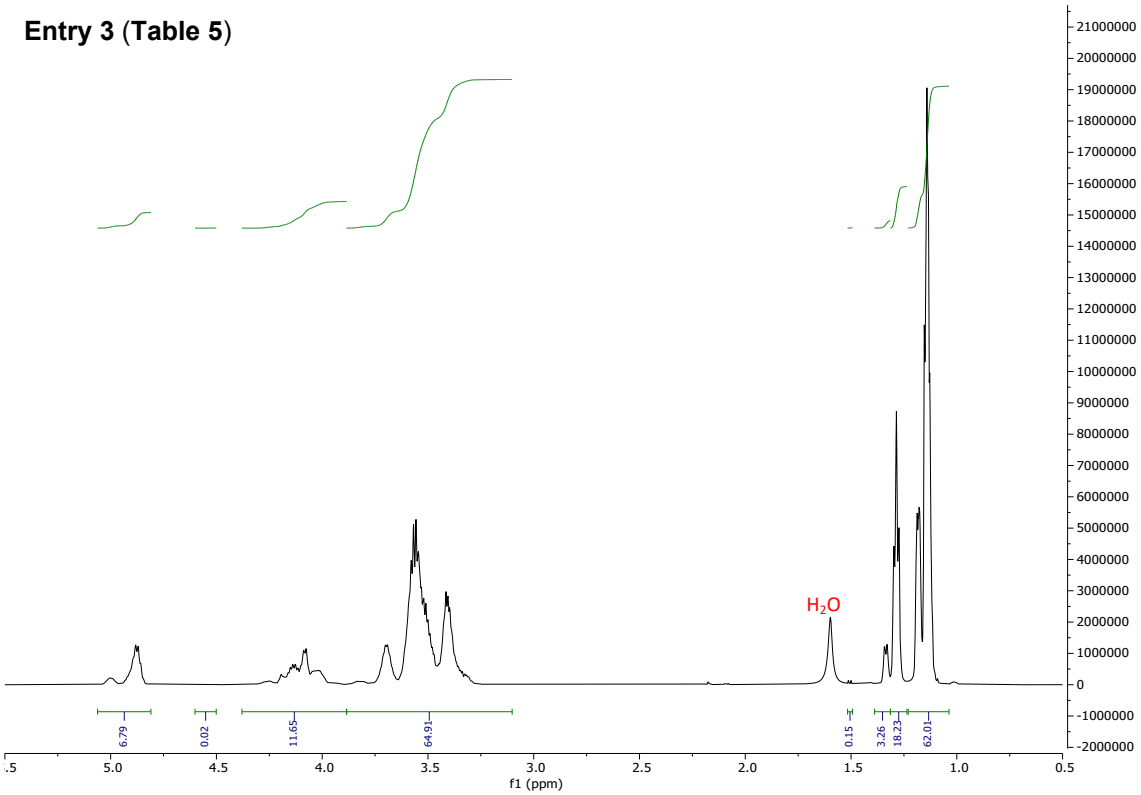


**Fig. S20.** $^{1}$H-NMR spectrum of the product derived from the Co-Ni catalyst at 90 ºC.

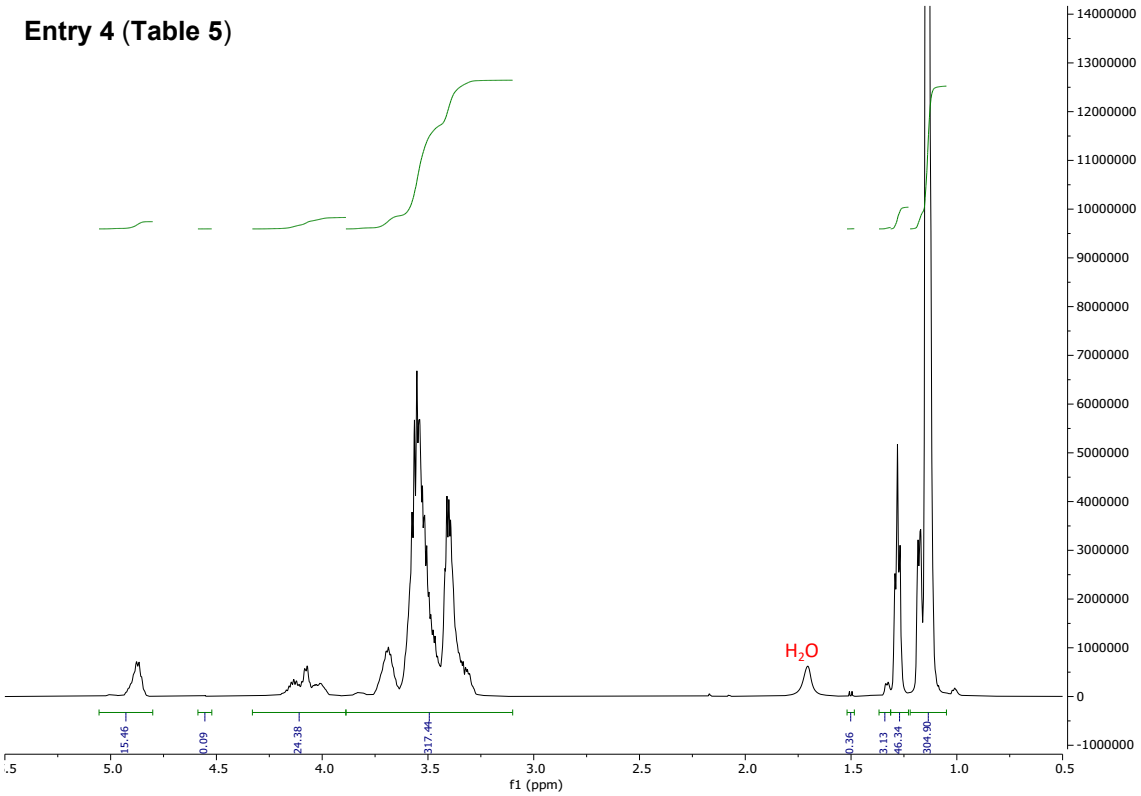


**Fig. S21.** $^{1}$H-NMR spectrum of the product derived from the Co-Ni catalyst at 120 ºC.

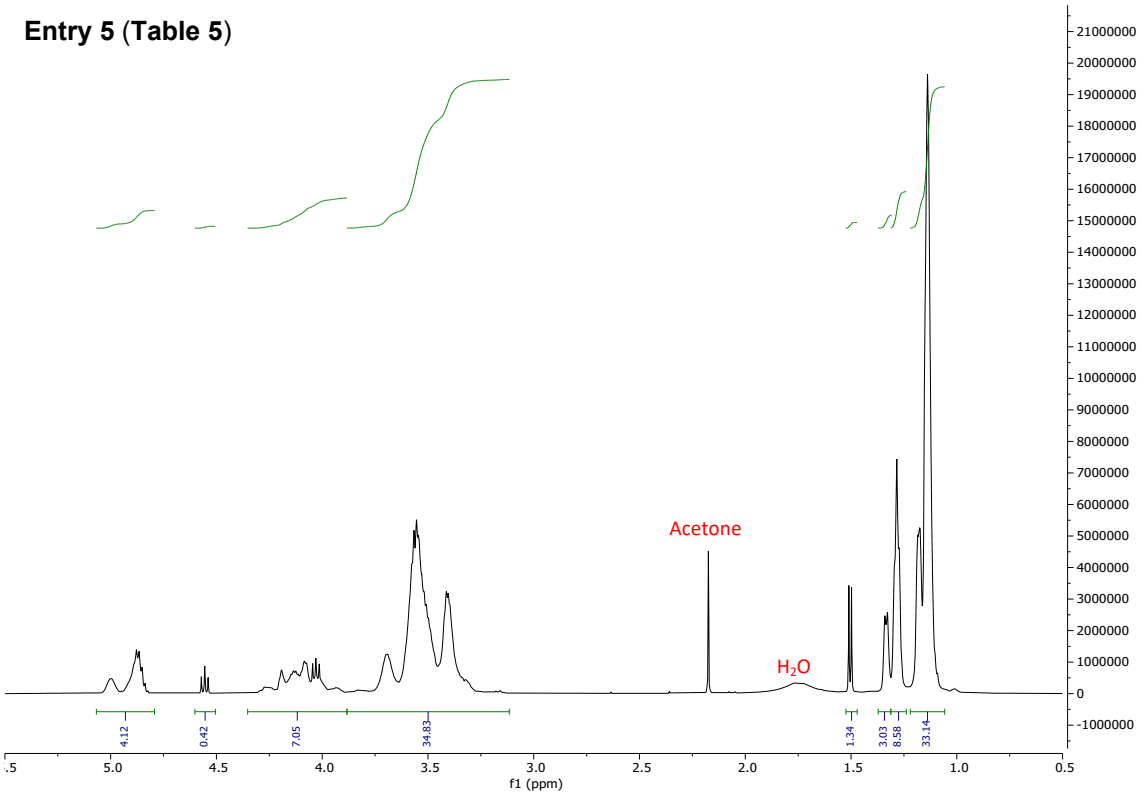


**Fig. S22.** $^1$H-NMR spectrum of the product derived from the Fe-Ni catalyst at 90 ºC.

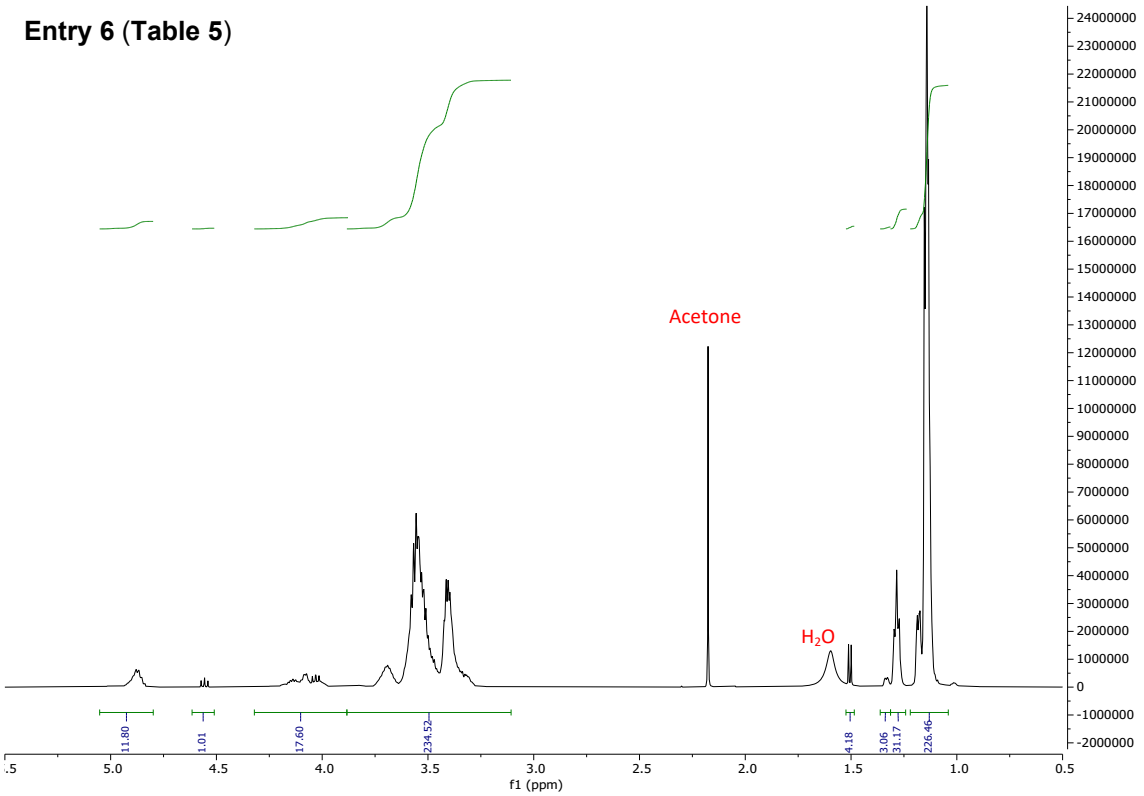


**Fig. S23.** $^1$H-NMR spectrum of the product derived from the Fe-Ni catalyst at 120 ºC.

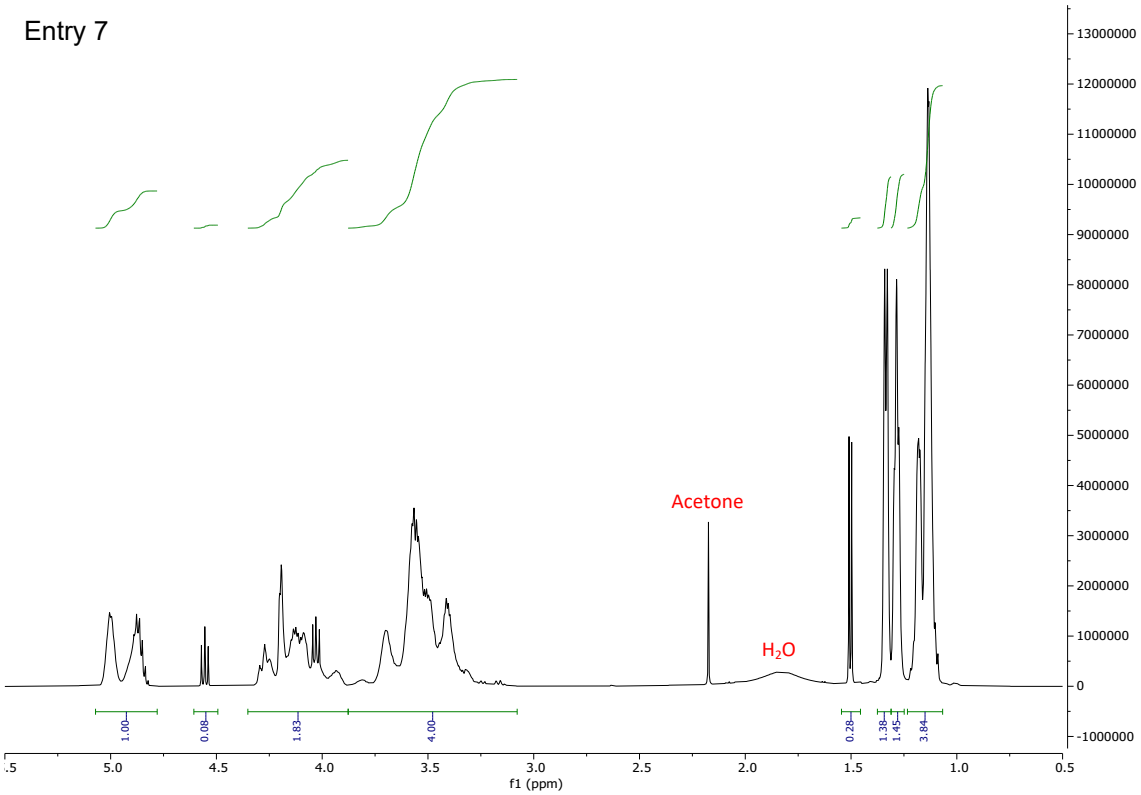


**Fig. S24.** $^1$H-NMR spectrum of the product derived from the Mn-Ni catalyst at 90 ºC.

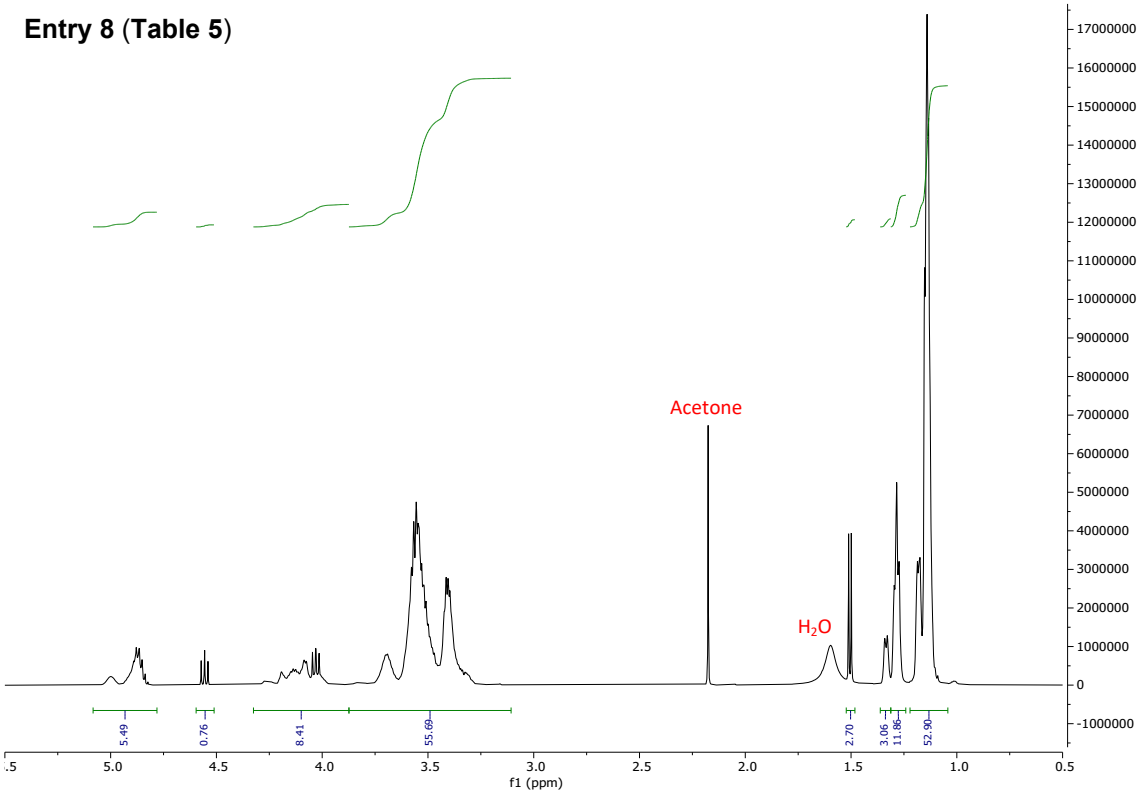


**Fig. S25.** $^1$H-NMR spectrum of the product derived from the Mn-Ni catalyst at 120 ºC.

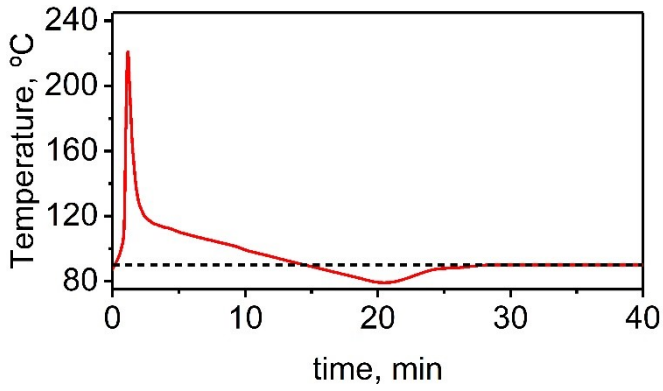


**Fig. S26.** Reactor temperature-time profiles for **entry 1** (**Table 5**).

After the induction period, the propagation rate becomes so rapid and the polymerization is so exothermic that the generated heat cannot be dissipated quickly enough, which leads to overheating. This temperature increase, in turn, triggers an autoacceleration process, causing the polymerization to reach maximum conversion in just a few minutes. However, such phenomenon negatively affects the catalytic performance of the Zn-Co DMC complex by i) deactivating it or reducing its activity,[6] ii) reducing $CO_2$ incorporation, iii) increasing PC production, iv) lowering molecular weights, and v) increasing dispersion.

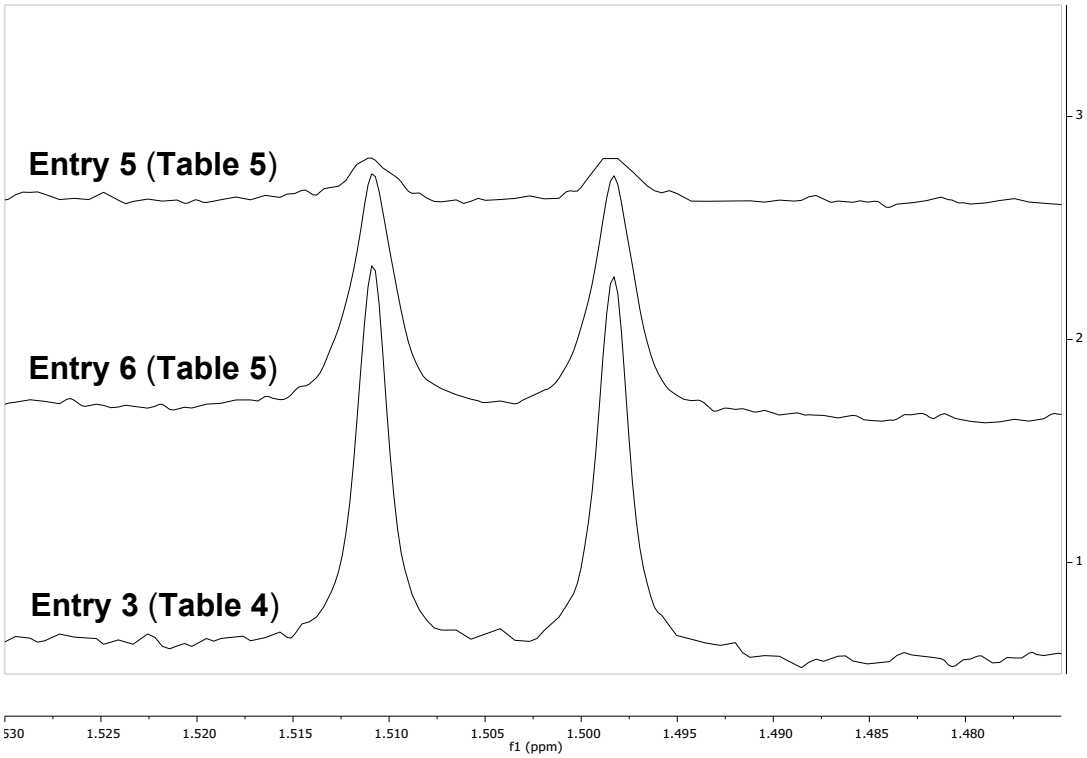


**Fig. S27.** $^1$H-NMR region corresponding to the methyl resonance of PC (1.475-1.53 ppm) for **entry 5** and **entry 6** (**Table 5**), and **entry 3** (**Table 4**).

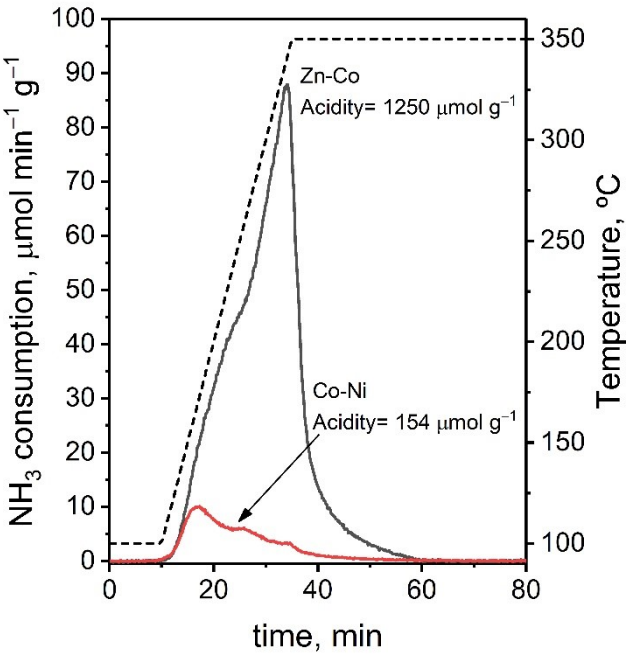


**Fig. S28.** $NH_3$-TPD profiles of the Zn-Co DMC and Co-Ni DMC complexes in the temperature range between 100 and 350 ºC.

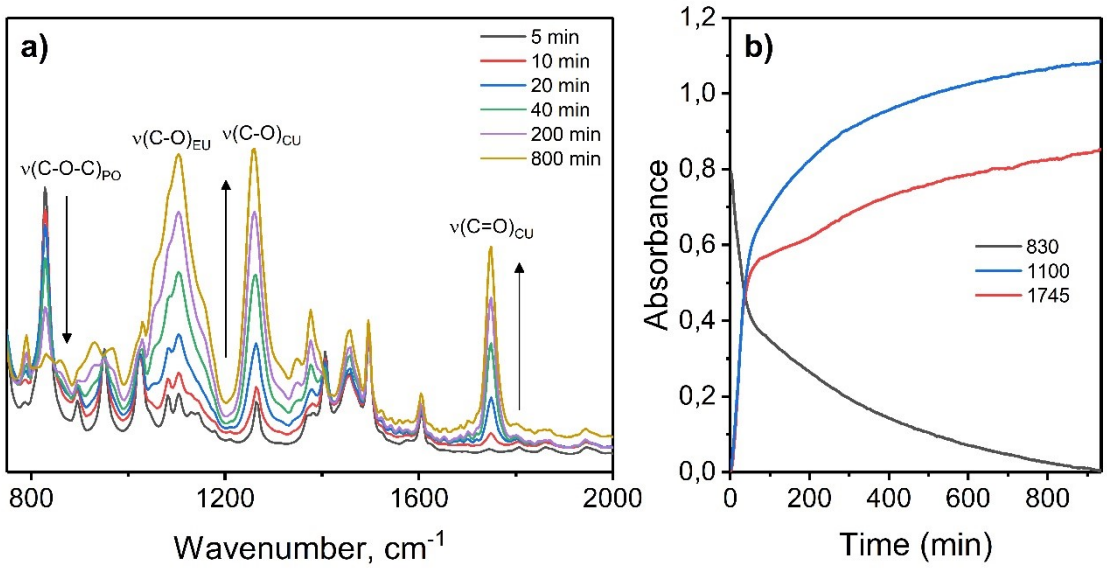


**Fig. S29. a)** IR spectra of reaction mixture during the copolymerization of $CO_2$ and PO in the presence of the Co-Ni DMC catalyst; **b)** *In situ* IR monitoring of absorbance profiles at frequencies indicated (in $cm^{-1}$).

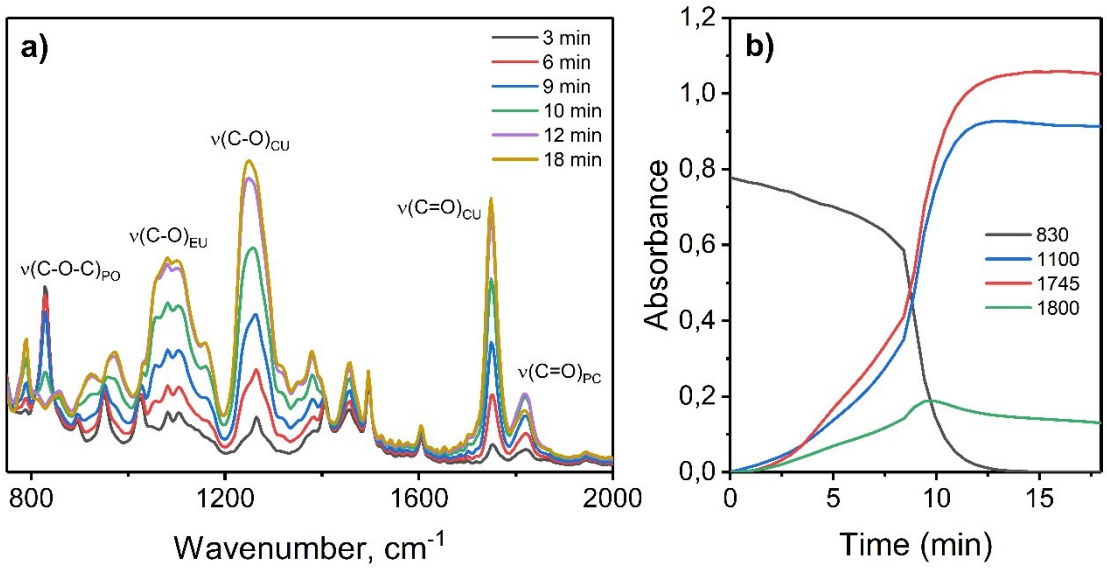


**Fig. S30.** IR spectra of reaction mixture during the copolymerization of $CO_2$ and PO in the presence of the Zn-Co DMC catalyst; **b)** *In situ* IR monitoring of absorbance profiles at frequencies indicated (in $cm^{-1}$). The profile at 800 $cm^{-1}$ correspond to the PO starting material, 1800 $cm^{-1}$ is the cyclic PC band, 1745 $cm^{-1}$ is the PPC carbonyl band, and 1100 $cm^{-1}$ is the PPC ether band.

The evolution of the concentration of PO in the reaction mixture can be calculated by following the evolution with time of the IR signal at 830 $cm^{-1}$, which is associated to the $\nu$(C-O-C) stretching mode of PO. According to the Beer-Lambert law, the absorbance of the peak at 830 $cm^{-1}$ at any time t ($A_t$), is directly proportional to the product of the molar absorptivity ($\varepsilon_{830}$), the optical path length (L) and the concentration of PO at such time t ($[PO]_t$).

$$A_t = \varepsilon_{830} \cdot L \cdot [PO]_t \tag{S8}$$

Of course, the equation can be also applied for t=0.

$$A_0 = \varepsilon_{830} \cdot L \cdot [PO]_0 \tag{S9}$$

Combining **eqn. (S8)** with **eqn. (S9)**, an expression is obtained that relates changes in the absorbance of the signal at 830 $cm^{-1}$ with changes in the concentration of PO:

$$\frac{A_t}{A_0} = \frac{[PO]_t}{[PO]_0} \tag{S10}$$

Therefore, the conversion of PO ($X_{PO}$) at each instant t can be calculated from the evolution of the absorbance of the peak at 830 $cm^{-1}$.

$$X_{PO} = 1 - \frac{[PO]_t}{[PO]_0} = 1 - \frac{A_t}{A_0} \tag{S11}$$

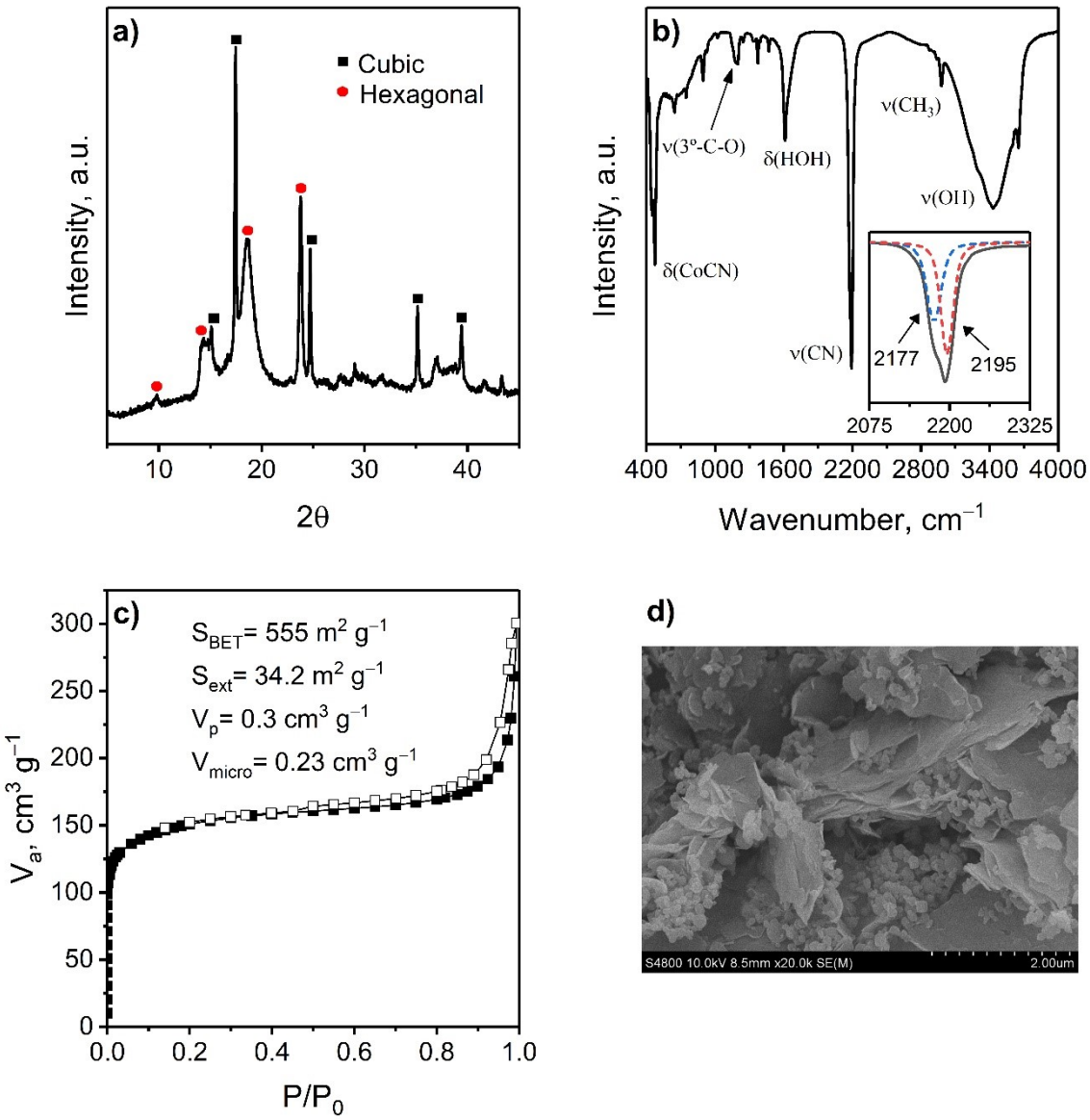


**Fig. S31.** Basic characterization of the Zn-Co DMC catalyst. **a)** XRD spectrum, **b)** FT-IR spectrum (Inset: ν(CN) spectral region), **c)** $N_2$ physisorption isotherm and **d)** SEM image.

The Zn-Co DMC complex employed was synthesized following the procedure described in the manuscript for the 2D layered DMC compounds.

According to the XRD pattern (**Fig. S27.a**), the material obtained was composed of two well-differentiated crystallographic phases. The expected 3D cubic lattice structure (■, ICDD 01-076-5029), in which both the $[Co(CN)_6]^{3-}$ molecular block and the $Zn^{2+}$ cation adopt a six-fold coordination, and a laminar structure with hexagonal unit cell (♦) in which the molecular block retains its octahedral coordination but $Zn^{2+}$ takes a tetragonal

coordination geometry. The layers extend in the ab-plane and are connected to each other by Cl atoms and/or TBA molecules.[7]

The coexistence of both crystallographic phases can be easily discerned by observing the v(CN) region of the IR spectrum (inset in **Fig. S27.b**). The deconvolution returns two peaks, one at 2177 $cm^{-1}$ associated with the cubic phase, and another at 2195 $cm^{-1}$ associated with the layered phase. In addition, in the FT-IR spectrum it can be observed how the Zn-Co DMC complex retains appreciable amounts of TBA in its structure, as well as water.

In $N_2$ adsorption-desorption isotherm (**Fig. S27.c**), a very large initial $N_2$ adsorption is observed, which warns of the presence of micropores in the structure. At the same time, a hysteresis loop of the type H4 is observed, which is related to narrow slit-like pores derived from aggregates of layered materials. [8]

The SEM image (**Fig. S27.d)** provides a clear view of the lamellar structure surrounded by small pseudo cubic particles.

## REFERENCES


1 Y. Zhang, *Inorg. Chem.*, 1982, 21, 3886-3889.

2 Y. Zhang, *Inorg. Chem.*, 1982, 21, 3889-3893.

3 R. L. McCullough, L. H. Jones, G. A. Crosby, *Spectrochim. Acta*, 1960, 16, 929-944.

4 D. P. Domonov, S. I. Pechenyuk, Y. P. Semushina*, J. Therm. Anal. Calorim.*, 2021, 146, 629-635.

5 C. Aparicio, L. Machala, Z. Marusak, *J. Them. Anal. Calorim.*, 2012, 110, 661-669.

6 I. Kim, J.T. Ahn, C. S. Ha, C. S. Yang, I. Park, *Polymer*, 2003, 44, 3417-3428.

7 N. Almora-Barrios, S. Pogodin, L. Bellarosa, M. García-Melchor, G. Revilla-López, M. García-Ratés, A. B. Vázquez-García, P. Hernández-Ariznavarreta, N. López, *ChemCatChem*, 2015, 7, 928-935.

8 K. S. W. Sing, D. H. Everett, R. A. W. Haul, L. Moscou, R. A. Pierotti, J. Rouquerol, T. Siemieniewska, *Pure & Appl. Chem.*, 1985, 57, 603-619.